

Low-energy cross section of the ${}^7\text{Be}(p, \gamma){}^8\text{B}$ solar fusion reaction from the Coulomb dissociation of ${}^8\text{B}$

F. Schümann,¹ S. Typel,² F. Hammache,^{2,*} K. Sümmerner,^{2,†} F. Uhlig,^{2,3} I. Böttcher,⁴ D. Cortina,^{2,‡} A. Förster,^{3,§} M. Gai,⁵ H. Geissel,² U. Greife,⁶ E. Grosse,⁷ N. Iwasa,⁸ P. Koczoń,² B. Kohlmeyer,⁴ R. Kulesa,⁹ H. Kumagai,¹⁰ N. Kurz,² M. Menzel,⁴ T. Motobayashi,^{10,||} H. Oeschler,³ A. Ozawa,^{10,||} M. Płoskoń,⁹ W. Prokopowicz,⁹ E. Schwab,² P. Senger,² F. Strieder,¹ C. Sturm,^{2,3} Zhi-Yu Sun,^{2,¶} G. Surówka,^{2,9} A. Wagner,⁷ and W. Walus⁹

¹*Institut für Physik mit Ionenstrahlen, Ruhr-Universität Bochum, D-44780 Bochum, Germany*

²*Gesellschaft für Schwerionenforschung, D-64220 Darmstadt, Germany*

³*Technische Universität Darmstadt, D-64289 Darmstadt, Germany*

⁴*Phillips-Universität Marburg, D-35032 Marburg, Germany*

⁵*University of Connecticut, Groton, Connecticut 06340, USA*

⁶*Department of Physics, Colorado School of Mines, Golden, Colorado 80401, USA*

⁷*Forschungszentrum Rossendorf, D-01314 Dresden, Germany*

⁸*Tohoku University, Aoba, Sendai, Miyagi 980-08578, Japan*

⁹*Jagellonian University, PL-30-059 Kraków, Poland*

¹⁰*RIKEN (Institute of Physical and Chemical Research), Wako, Saitama 351-0198, Japan*

¹¹*Rikkyo University, Toshima, Tokyo 171, Japan*

(Received 15 August 2005; published 27 January 2006)

An exclusive measurement of the Coulomb breakup of ${}^8\text{B}$ into ${}^7\text{Be}+p$ at 254A MeV was used to infer the low-energy ${}^7\text{Be}(p, \gamma){}^8\text{B}$ cross section. The radioactive ${}^8\text{B}$ beam was produced by projectile fragmentation of 350A MeV ${}^{12}\text{C}$ and separated with the FRagment Separator (FRS) at Gesellschaft für Schwerionenforschung in Darmstadt, Germany. The Coulomb-breakup products were momentum-analyzed in the KaoS magnetic spectrometer; particular emphasis was placed on the angular correlations of the breakup particles. These correlations demonstrate clearly that $E1$ multipolarity dominates within the angular cuts selected for the analysis. The deduced astrophysical S_{17} factors exhibit good agreement with the most recent direct ${}^7\text{Be}(p, \gamma){}^8\text{B}$ measurements. By using the energy dependence of S_{17} according to the recently refined cluster model for ${}^8\text{B}$ of P. Descouvemont [Phys. Rev. C **70**, 065802 (2004)], we extract a zero-energy S factor of $S_{17}(0) = 20.6 \pm 0.8(\text{stat}) \pm 1.2(\text{syst})$ eV b. These errors do not include the uncertainty of the theoretical model to extrapolate to zero relative energy, estimated by Descouvemont to be about 5%.

DOI: [10.1103/PhysRevC.73.015806](https://doi.org/10.1103/PhysRevC.73.015806)

PACS number(s): 25.40.Lw, 25.60.-t, 25.70.De, 26.65.+t

I. INTRODUCTION

The so-called solar neutrino problem has been solved by the results of an experiment conducted at the Sudbury Neutrino Observatory (SNO) [1,2]. The SNO experiment shows strong evidence that the neutrino-flux deficit measured in charged-current interactions is a result of neutrino flavor oscillations between electron-neutrino production in the Sun and their detection on Earth. The flux measured in neutral-current interactions of high-energy solar neutrinos is in general agreement with the flux predicted by the standard solar model (SSM, Refs. [3,4]). The current slight discrepancy between the flux predicted by the SSM and the neutral-current flux measured by SNO [2] may be significant or not depending on the uncertainty of the flux prediction; e.g., a small but significant deficit could be evidence for oscillations into sterile

neutrinos. To that end, it is essential to further reduce the uncertainty of nuclear inputs to the SSM in order to refine its predictions. One critical quantity is the ${}^7\text{Be}(p, \gamma){}^8\text{B}$ cross section at solar energies since it is linearly related to the high-energy solar neutrino flux stemming from ${}^8\text{B}$ β decay.

In recent years, many attempts have been undertaken to measure this cross section with high precision in direct-proton-capture measurements using radioactive ${}^7\text{Be}$ targets [5–8]. Unfortunately, these results do not yield a completely consistent picture: The earlier measurements (Refs. [5,6]) yield lower zero-energy astrophysical S factors, $S_{17}(0)$, around 19 eV b, whereas the two more recent ones (Refs. [7,8]) obtain results which are about 15% higher. All (p, γ) data sets, however, were found to be consistent with an energy dependence of S_{17} as given by the cluster model of Descouvemont and Baye [9].

In view of their importance to astrophysics and elementary-particle physics, these results should be cross-checked by other, indirect measurements that have different systematic errors. One possibility is Coulomb dissociation (CD) of ${}^8\text{B}$ in the electromagnetic field of a high- Z nucleus. Such measurements have been performed at intermediate [10,11] and high [12] energies. The present paper reports on a CD experiment similar to that of Iwasa *et al.* (GSI-1, Ref. [12]),

*Present address: IPN Orsay, F-91406 Orsay Cedex, France.

†Corresponding author: k.suemmerer@gsi.de

‡Present address: Universidad Santiago de Compostela, Spain.

§Present address: CERN, CH-12211 Geneve 23, Switzerland.

||Present address: University of Tsukuba, Ibaraki, Japan.

¶Present address: Inst. of Modern Physics, Lanzhou, China.

but with an improved experimental technique: In GSI-1, the incident ^8B beam could not be tracked before the target, whereas in the present run we could measure the angles before and after the target with good precision. Preliminary results of the present study were published earlier [13]. For the present publication, the data were reanalyzed, leading to slightly different results for the lowest-energy data points.

Another indirect method used to deduce $S_{17}(0)$ is to determine the asymptotic normalization coefficients (ANC) of the proton wave functions bound in the ^7Be potential. This method makes use of the fact that because of the very low proton binding energy, radiative proton capture is extremely peripheral and $S_{17}(0)$ can be calculated directly from the ANC. These ANC are determined from low-energy proton-transfer or from proton-removal cross sections [14–16]. A recent reexamination of ANC results for $^7\text{Be}(p, \gamma)$ by Trache *et al.* yielded a relatively small central value of $S_{17}(0) = 18.7 \pm 1.9 \text{ eV b}$ [15]. Still, this value is in line with all published values of $S_{17}(0)$ except for Ref. [8].

It is important to compare the results from direct and indirect methods to determine the astrophysical S factors with each other since the indirect methods could also be used to study astrophysically interesting reactions between *unstable* nuclei where direct-capture reactions cannot be applied. The reaction $^7\text{Be}(p, \gamma)^8\text{B}$ could be an ideal test case, provided that the remaining inconsistencies in $S_{17}(0)$ from the different direct and indirect methods can be resolved.

In the present paper, we give a comprehensive report of the CD experiment performed at Gesellschaft für Schwerionenforschung (GSI) [13] where we impinged a secondary ^8B beam with an incident energy of 254A MeV on a ^{208}Pb breakup target. As already mentioned in our earlier publication, we focus on a crucial question that must be answered if one wants to use the CD method to derive a precise value for $S_{17}(0)$: the contribution of $E2$ multipolarity to CD of ^8B . One can calculate that $E1$ is the dominant multipolarity in CD as well as in direct proton capture, but it is obvious that the equivalent photon field from a high- Z target nucleus seen by a projectile at a few hundred MeV per nucleon contains also a strong $E2$ component. Experimental limits for a possible $E2$ contribution were extracted in the work of Kikuchi *et al.* [10] and Iwasa *et al.* [12]; both papers found negligible $E2$ contributions. Recently, Davids *et al.* have reported positive experimental evidence for a finite $E2$ contribution in CD of ^8B , mainly from the analysis of *inclusive* longitudinal momentum ($p_{||}$) spectra of ^7Be fragments measured at 44 and 81A MeV [11,17]; they therefore subtracted a calculated $E2$ contribution from their S_{17} data. In order to resolve these discrepancies, we analyzed observables that should be particularly sensitive to contributions from $E2$ multipolarity, namely, the angular correlations of the ^8B -breakup particles, namely, proton and ^7Be .

II. MODEL CALCULATIONS

Accurate model calculations of the CD of ^8B are essential for several reasons. From a practical point of view, the relatively bad energy resolution of the CD method requires one to simulate, e.g., the effects of cross talk between

neighboring energy bins, of the finite size and resolution of the tracking detectors, etc. These simulations require a CD event generator that is reasonably close to reality so that the remaining differences between the measured and simulated cross-section distributions can be attributed to the S_{17} factor. For this purpose, we have used a simple potential model of ^8B .

Since the current experiment [like most other direct and indirect studies of the $^7\text{Be}(p, \gamma)^8\text{B}$ reaction] does not allow us to measure at solar energies, the data set has to be extrapolated toward $E_{\text{rel}} = 0$. For this purpose, we have to use the most sophisticated model available. We will show below that a cluster model of ^8B [18] seems to be best suited for a reliable extrapolation.

A. Nuclear structure of ^8B

The isotope ^8B has one of the lowest proton binding energies of all particle-stable nuclei known in the chart of nuclides ($B_p = 137.5 \text{ keV}$ [19]). The relevant parts of the ^7Be and ^8B level schemes are depicted in Fig. 1. The simplest model for ^8B is that of a p -wave proton coupled to an inert ^7Be core with $I^\pi = 3/2^-$ to form the ^8B ground state with $I^\pi = 2^+$. We adopted this simplified single-particle model of ^8B to calculate cross sections within the simulations described below. Details of the model are described in Ref. [17]. The proton is bound in a Woods-Saxon potential with radius parameter $r_0 = 1.25 \text{ fm}$ and diffuseness $a = 0.65 \text{ fm}$. As usual, the p -wave potential depth has been adjusted to match the ^8B proton binding energy; this yields a depth of 43.183 MeV. The s -, d -, and f -wave potentials have been adjusted to reproduce the s -wave scattering lengths of the mirror $^7\text{Li}+n$ reaction [20], this yields $V_1 = 43.857 \text{ MeV}$ for channel spin $S = 1$ and $V_2 = 52.597 \text{ MeV}$ for channel spin $S = 2$. We note that we obtain for the dominant channel spin $S = 2$, an s -wave scattering length for $^7\text{Be}+p$ of $a_{02}^{\text{theo}} = -8 \text{ fm}$, which agrees well with the recently measured value of $a_{02}^{\text{exp}} = -7 \pm 3 \text{ fm}$ (Angulo *et al.* [21]).

With this model, we obtain astrophysical S factors as a function of the proton- ^7Be relative energy E_{rel} , as shown in Fig. 2. The nonresonant direct capture into the ^8B ground

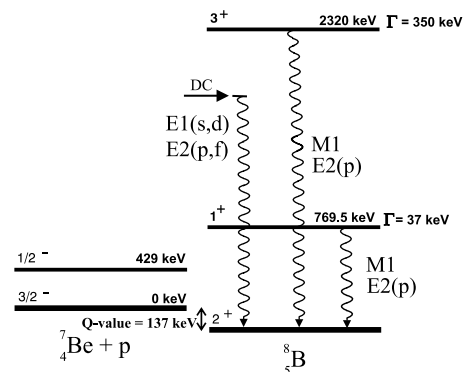


FIG. 1. Level schemes of ^7Be and ^8B relevant to direct proton capture into the ground state of ^8B and to resonant capture via the $M1$ resonances at 0.770 and 2.32 MeV excitation energies.

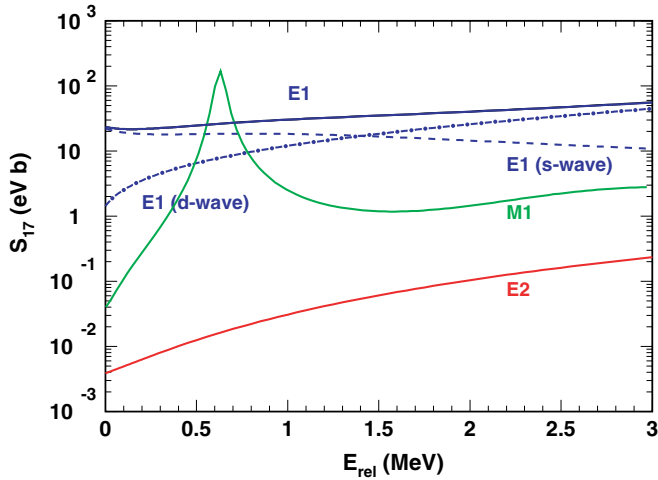


FIG. 2. (Color online) Theoretical S_{17} factors from a simple potential model of ${}^8\text{B}$ and their decomposition into contributions from various partial waves.

state proceeds mainly via s - and d -wave captures and $E1$ γ emission. Capture of p and f waves followed by $E2$ emission plays an insignificant role, in particular at solar energies. The resonant component proceeds through the 1^+ resonance at 770 keV (632 keV above threshold), which decays mainly by $M1$ emission and is limited essentially to a narrow region around the resonance energy, with minor but finite contributions at relative energies above the resonance. The $M1$ resonance cross section has been obtained from experimental data [22]; it is not contained in the model of Ref. [17]. We ignored entirely the high-lying $M1$ resonance at 2.32 MeV since it cannot be seen in our high-energy CD experiment, because of both the small cross section in CD and its large width.

The potential model of ${}^8\text{B}$ sketched above ignores the well-known cluster structure of ${}^7\text{Be}$ (see, e.g., Ref. [23]). Descouvemont and Baye [9] have therefore applied a model where ${}^8\text{B}$ is assumed to consist of, e.g., $p+({}^7\text{Be} = {}^3\text{He}+{}^4\text{He})$ or ${}^3\text{He}+({}^5\text{Li} = p+{}^4\text{He})$ three-cluster structures, including excited states of the clusters. Later, this model was slightly refined [18] by allowing also for variations in the cluster separation and by using different effective nucleon-nucleon interactions; the results were found to be largely unchanged. Our potential model can be viewed as a simplification of the cluster model where the cluster distance is artificially set to zero; the spectroscopic information available for ${}^7\text{Be}$, however, points to a finite cluster distance of ≈ 3.5 fm [18].

For computational simplicity, we will use the potential model to simulate the differential observables in our experiment and come back to the cluster model at the end of this article, where we discuss the extrapolation of S_{17} toward zero relative energy.

B. Coulomb dissociation of ${}^8\text{B}$

As proposed by Baur *et al.* [24], CD can be used favorably to measure radiative-capture cross sections by making use of the strong flux of equivalent photons originating from

a heavy target nucleus as seen by a fast-moving projectile, which replaces the presently insufficient intensity of available real-photon sources. Assuming first-order perturbation theory for the electromagnetic excitation process, CD cross sections can be converted directly to photodissociation cross sections. The latter are related to the astrophysically relevant radiative-capture cross sections by the principle of detailed balance. It is obvious that the indirect method of CD needs theoretical input in the conversion process.

There are several sources for complications. They can be identified and minimized by selecting appropriate observables and kinematical conditions in the experiment.

- (i) Several multiplicities ($E1$, $E2$, $M1$, ...) with different weights contribute in radiative capture reactions and Coulomb breakup. In principle, they can be disentangled by studying angular distributions in CD, preferably in the center-of-mass system of the excited nucleus. Their relative strengths depend on projectile energy and scattering angle.
- (ii) An exchange of more than one photon (higher-order effects) destroys the direct relation between the CD cross section and the photodissociation cross section. High projectile energies and large impact parameters reduce this effect.
- (iii) The nuclear interaction between projectile and target induces nuclear breakup and absorption. It becomes relevant for small impact parameters.

These are general features of CD that can be included in the theoretical description of the breakup mechanism in various approximations which lead to corrections of the simple pure-Coulomb first-order approach.

1. Semiclassical calculations

The Coulomb-breakup mechanism can be described in both fully quantal approaches and semiclassical models [25]. In the latter case, the projectile is assumed to move on a classical trajectory with respect to the target. In our case, we use the semiclassical model in first-order perturbation theory (PT) to describe the CD of ${}^8\text{B}$ in the Coulomb field of ${}^{208}\text{Pb}$, as described in more detail elsewhere [17,26,27]. The excitation amplitude is calculated in the relativistic approach assuming a straight-line trajectory but correcting the excitation functions for the deflection in the Coulomb field of the target [28]. This is appropriate at the high incident energy used in the present experiment (254A MeV) and justified *a posteriori* by the good agreement with the measured angular distributions.

In addition to CD, nuclear overlap of ${}^8\text{B}$ and ${}^{208}\text{Pb}$ has to be considered. This will mainly take flux out of the ${}^7\text{Be}+p$ exit channel; feeding this channel by nuclear interaction has been calculated to be of minor importance by Bertulani and Gai [29]. In order to take nuclear absorption into account, we modified the relativistic Coulomb-excitation functions by multiplying them with a correction factor as described in Ref. [27]. This factor is derived from an eikonal approximation of the excitation functions taking both Coulomb and nuclear potentials into account. In the present case, we assume a diffuse

absorptive nuclear potential with a depth of 20 MeV and a radius of 9.91 fm, i.e., the sum of the projectile and target radii. As we will see below, this choice reproduces well the integral scattering-angle distribution.

2. Dynamical calculations

Higher-order effects from the exchange of more than one photon can be considered in semiclassical calculations that study the time evolution of the projectile system during the scattering. As compared to a first-order calculation, the momenta of the outgoing particles are modified in the Coulomb field of the target leading to a distortion of relative-energy and angular-momentum distributions. Esbensen *et al.* [30,31] have proposed that discrepancies between the results from radiative-capture and CD studies of the ${}^7\text{Be}(p, \gamma){}^8\text{B}$ reaction are due to deficiencies of the method in evaluating S_{17} from CD cross sections by using first-order PT. They point out that a full dynamical calculation of CD, if compared to a first-order PT calculation, will lead to an increased S_{17} factor at low E_{rel} and a reduced one at high E_{rel} , thus producing a smaller slope of S_{17} vs. E_{rel} and a better agreement between the results from the two methods. However, the amount of this modification depends on the assumed $E2$ strength and thus is model dependent. Recently, fully quantal calculations became available that consider the post-acceleration of the fragments in the Coulomb field of the target. In contrast to dynamical calculations in the semiclassical approach, they predict an *increase* in the cross section at low relative energies [32]. More theoretical work is required to obtain a consistent picture of higher-order effects.

To follow the suggestions of Esbensen *et al.*, we also performed dynamical calculations of the CD of ${}^8\text{B}$ at 254A MeV following the approach described in Ref. [17] for lower projectile energies assuming the simple potential model for ${}^8\text{B}$. The ${}^8\text{B}$ nucleus moves on a Coulomb trajectory taking the deflection into account. $E1$ and $E2$ multipoles were considered in the standard far-field approximation with the full strength as predicted by the model.

In both theoretical approaches, triple-differential cross sections for the CD of ${}^8\text{B}$ are obtained. These distributions of observables cannot be compared directly to the measured data, but have to be folded with the respective experimental resolutions. To this end, the cross sections were converted to statistically distributed “event” distributions from both (PT and dynamical) calculations and run through our experimental filter, as will be described in more detail below.

III. EXPERIMENTAL PROCEDURES

Several other CD studies of ${}^8\text{B}$ breakup [10,11] have used intermediate energies between 46 and 83A MeV as available from cyclotron-based radioactive-beam facilities. At GSI, the 18 Tm heavy-ion synchrotron, SIS-18, allows the use of a much higher incident energy. We chose a ${}^8\text{B}$ incident energy of 254A MeV limited by the maximum bending power of the KaoS spectrometer used for determining the momenta of the breakup particles p and ${}^7\text{Be}$. In the following we will describe

in detail the preparation and identification of the secondary beam as well as the experimental equipment used to measure the breakup.

A. Preparation and properties of the ${}^8\text{B}$ beam

The ${}^8\text{B}$ secondary beam was produced at the FRagment Separator (FRS) at GSI [33] by fragmenting a 350A MeV ${}^{12}\text{C}$ beam in an 8 g/cm² Be target and separating it from contaminant ions in a 1.4 g/cm² wedge-shaped Al degrader placed in the FRS intermediate focal plane.

Typical ${}^8\text{B}$ beam intensities in front of KaoS were 5×10^4 per 4 s spill; the only contaminant consisted of about 20% ${}^7\text{Be}$ ions which could be identified event by event with the help of a time-of-flight (TOF) measurement. For this purpose, a 3 mm thick plastic scintillator detector was installed in the transfer line between FRS and KaoS, about 85 m upstream from the breakup target, to serve as a TOF start detector. Positions and angles of the secondary beam incident on the Pb breakup target were measured with the help of two parallel-plate avalanche counters (PPACs) located at 308.5 and 71 cm upstream from the target. The detectors, which were designed and built at RIKEN [34], had areas of 10×10 cm² and were allowed to track the incident ${}^8\text{B}$ beam with about 99% efficiency and with position and angular resolutions of 1.3 mm and 1 mrad, respectively. In addition, they provided a TOF stop signal with a resolution of 1.2 ns full width at half maximum (FWHM). Figure 3 shows a two-dimensional plot of the TOF between the scintillator detector and the second PPAC detector in front of the target. One can see that a TOF measurement alone is sufficient to separate the ${}^8\text{B}$ beam from contaminants on an event-by-event basis.

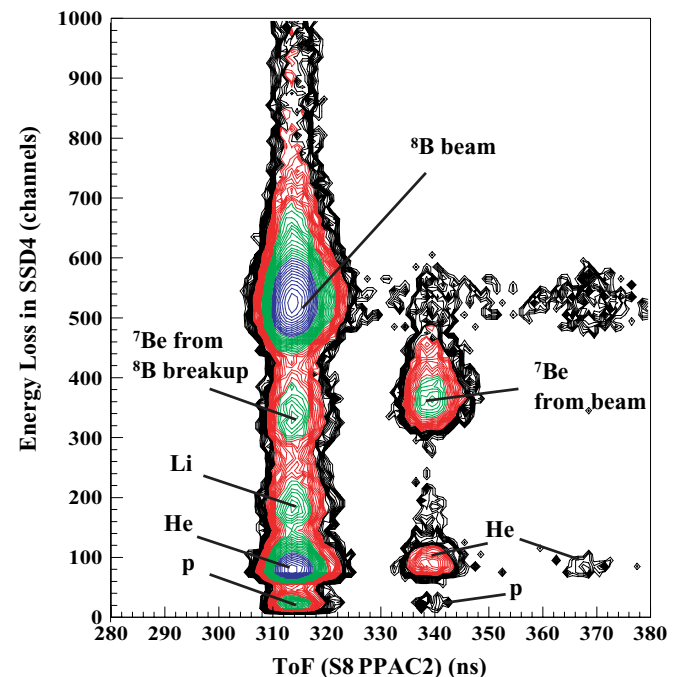


FIG. 3. (Color online) Identification of primary and secondary fragments by energy loss and time of flight.

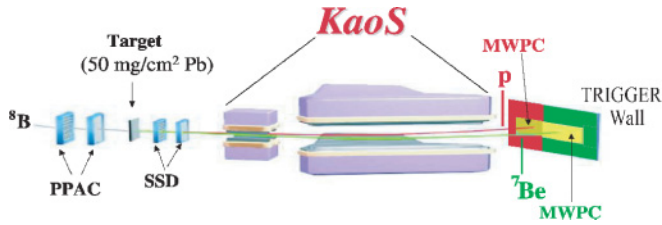


FIG. 4. (Color online) Experimental setup shows PPACs in front of and the fragment-tracking SSDs behind the Coulomb-breakup target. Proton and ${}^7\text{Be}$ positions in the focal plane of the KaoS magnetic spectrometer are determined by large-area MWPCs followed by a scintillator-paddle wall for trigger purposes.

B. Detection of breakup fragments

A schematic view of the experimental setup to detect the breakup of ${}^8\text{B}$ in semicomplete kinematics (i.e., without detecting coincident γ rays) at the KaoS spectrometer at GSI is shown in Fig. 4. Apart from the PPAC tracking detectors mentioned above, it consisted of (i) the ${}^{208}\text{Pb}$ breakup target, (ii) two pairs of Si strip detectors, (iii) the magnets of the KaoS spectrometer, (iv) two large-area multiwire proportional chambers (MWPCs), and (v) a TOF wall serving as a trigger detector. The individual components will be discussed in detail below.

1. Fragment tracking: Si strip detectors

Downstream from the Pb target (which consisted of 52 mg/cm^2 ${}^{208}\text{Pb}$ enriched to $99.0 \pm 0.1\%$ and had an area of 24 mm in height times 36 mm in width), the angles and positions as well as the energy losses of the outgoing particles were measured with two pairs of single-sided Si strip detectors (SSDs). These detectors (300 μm thick, 100 μm pitch) were located at distances of about 15 and 30 cm downstream from the target. Figure 5 shows schematically the layout of the SSD array. The vacuum of the beamline housing the PPACs, the target, and the SSDs was separated downstream from ambient air by a stainless-steel window of 50 μm thickness.

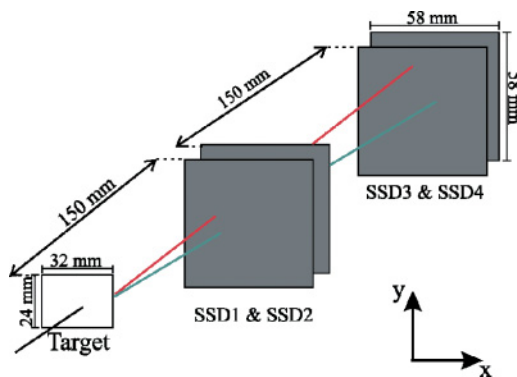


FIG. 5. (Color online) Geometrical arrangement of the four layers of single-sided SSDs yielding the breakup particles' trajectories directly after the target.

2. The KaoS magnetic spectrometer

The KaoS magnetic spectrometer [35] consisted of a large-aperture quadrupole and a horizontally focusing dipole magnet. The ratio between the smallest and largest momentum accepted by KaoS amounted to about 2, making KaoS an ideal instrument to detect breakup of neutron-deficient nuclei into a proton with $A/Z = 1$ and an ion with $A/Z \approx 2$. Prior to our measurement, the magnetic field of the KaoS dipole had been mapped in three dimensions to obtain an empirical field map; this map was then used to simulate the passage of charged particles through the magnet using the code GEANT-3 [36]. To avoid multiple scattering of the fragments in air, the chamber inside the quadrupole and dipole magnets was filled with He gas at 1 bar pressure, separated from the ambient air by thin He-tight foils.

3. Fragment tracking: Multiwire chambers and trigger detectors

Behind the magnets, two large-area MWPCs were installed as close to the focal plane as possible. One chamber, with horizontal and vertical dimensions of 60 and 40 cm, respectively, detected the positions of protons behind KaoS. The other one, 120 cm wide and 60 cm high, was set to detect the ${}^8\text{B}$ noninteracting beam and the ${}^7\text{Be}$ fragments. The separation of the position measurements of protons and the heavy ions allowed us to optimize each detector voltage for optimum detection efficiency.

Behind the focal plane and parallel to it, a plastic-scintillator wall with 30 elements (each 7 cm wide and 2 cm thick) was installed and used for trigger purposes. The wall was subdivided into two sections covering the respective MWPC in front of them. Coincident signals in the left-hand (proton) part and in the right-hand (ion) part of the wall indicated a breakup event (breakup trigger). Single hits in the right-hand section were interpreted as beam triggers and recorded with a down-scale factor of 1000.

C. Monte Carlo simulations

Monte Carlo simulations of the Coulomb breakup of ${}^8\text{B}$ and the detection of the breakup products were an indispensable part of the present experiment. They were essential in planning the experiment, helped to estimate the energy resolution and detection efficiencies, and were instrumental in determining the proton and ${}^7\text{Be}$ momenta from the measured positions. As a tool for these Monte Carlo simulations, the program package GEANT-3 [36] was used.

The Monte Carlo simulations started with an event generator that simulated CD of ${}^8\text{B}$ on ${}^{208}\text{Pb}$ in first-order perturbation theory or via a fully dynamical calculation by the theoretical approaches mentioned above (Sec. II B). Technically, the event generator produced statistically distributed ensembles of 500 000 CD "events" each that were used as input to a GEANT simulation of the passage of each breakup particle through the Pb target, the SSD detectors, the beamline exit window, the He-filled interior of the magnets, and the air behind KaoS before hitting the MWPC volumes. At the target, the emittance

of the ^8B as measured with the PPACs was imposed, and the momentum spread was assumed to be the nominal FRS momentum acceptance $\Delta p/p = \pm 1\%$.

Momenta of each particle type (p , ^7Be , ^8B) were obtained from two position measurements in the SSD and one position measurement in the respective MWPC. To calculate each particle type's momentum, a 36-term polynomial expression was derived; its parameters were obtained in a GEANT simulation by sending particles with known momenta (covering evenly the range of relevant momenta) through the setup and fitting the momenta as a function of the positions by varying the 36 polynomial parameters. In a similar way, the invariant-mass resolution of the experiment could be obtained by simulating breakup events of known invariant mass and reconstructing this quantity from the simulated positions. The top panel in Fig. 6 shows the E_{rel} resolution (1σ width) as a function of the p - ^7Be relative energy E_{rel} as determined from the simulation.

The efficiency of our setup at high E_{rel} is mainly given by the finite sizes of the SSD and MWPC detectors. Below the maximum around 0.5 to 1 MeV, the efficiency drops because of overlap of the proton and ^7Be hit patterns in the SSD leading to apparent multiplicity 1 instead of 2. Numerical values of the efficiency could be obtained by simulating the full set of 500 000 CD events with and without the above conditions and plotting the ratios of these numbers for different, evenly spaced E_{rel} bins. This distribution is shown in the lower panel of Fig. 6. The upper set of data points (circles) was obtained by requiring two separated p -Be hits inside all detector volumes.

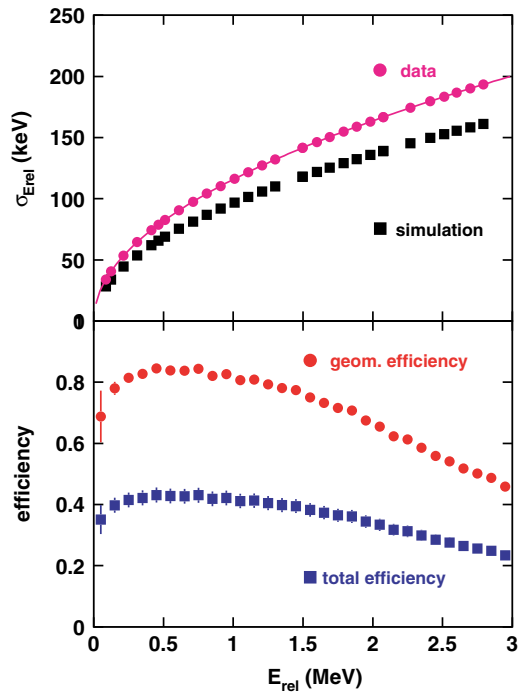


FIG. 6. (Color online) Calculated properties of the experimental setup from GEANT simulations. Top: E_{rel} resolution (squares). Upper set of points (circles) was determined from the experimental data. Bottom: Geometrical efficiency (upper set of data points). Lower set of data points shows the total efficiency including all analysis conditions.

The lower set of data points (squares) was obtained by taking into account the intrinsic detector and trigger efficiencies and applying all analysis conditions, see Sec. IV B below. It can be seen that the major part of the E_{rel} distribution is covered with high total efficiency (about 30–40%). It should be noted that this curve is insufficient to correct measured data for efficiency. The total efficiency is a multidimensional function of both the original and the smeared-out (by the experimental resolution) angles and momenta of both particles. Therefore, we pass the theoretical “events” through the experimental filter and compare the results to the same quantities derived from the data.

IV. DATA REDUCTION AND RESULTS

This experiment recorded events from three different sources:

- (i) Breakup events originating in the Pb target,
- (ii) Down-scaled beam particles, and
- (iii) Background from a variety of sources (e.g., cosmic rays).

Though event classes (i) and (ii) are mainly correlated with a corresponding trigger type [breakup trigger for class (i), beam trigger for class (ii)], we checked if by chance the trigger types and event classes were mixed in rare cases and corrected for that.

In the following, we first show how the total number of incident ^8B projectiles is obtained from the beam trigger events. We then explain how the breakup events originating in the Pb target were identified.

A. Total number of ^8B projectiles

The absolute number of ^8B ions impinging on the ^{208}Pb breakup target needs to be known to determine absolute cross sections. To this end, beam trigger events were analyzed to select those that correspond to ^8B in the ΔE -TOF plot, Fig. 3. A 3σ window around the ^8B energy-loss peak in each SSD was chosen. To convert the integrated number in this spectrum to the total number of incident ^8B ions, the down-scale factor of the beam trigger (10^3) and the efficiencies for detecting ^8B ions in the TOF detectors (3 mm scintillator, PPAC detectors) as well as in the ΔE (SSD) detectors have to be taken into account. These numbers were derived from sets of linear equations containing the coincidence count rates and the respective efficiencies. A small number (0.48%) of ^8B ions was found for the breakup trigger condition because of random-noise coincidences with the left (proton) part of the plastic-scintillator wall. Together with the total from the beam trigger condition we obtain a total of $(4.15 \pm 0.03)10^9$ ^8B ions impinging on the breakup target.

B. Identification and tracking of breakup products

The coincident p and ^7Be signals resulting from breakup in the ^{208}Pb target were identified among the class (i) events (breakup trigger) in several successive steps:

- (i) The ΔE -TOF condition was applied to select only incident ^8B ions (see above).

- (ii) A multiplicity of $m \geq 2$ in each SSD was required. That meant that at least one empty strip was found between two adjacent hit clusters.
- (iii) A 3σ window around the ΔE peak corresponding to the energy loss of ${}^7\text{Be}$ in each SSD selected ${}^7\text{Be}$ as one of the reaction products.
- (iv) The coincident protons were found among all events with $\approx 50 < \Delta E < 500$ keV in each SSD where the trajectories had a closest distance to the coincident ${}^7\text{Be}$ trajectory inside a volume given in x and y by the size of the target (± 18 mm in x and ± 12 mm in y direction) and in z direction (along the beam axis) of ± 25 mm around the target (located at $z = 0$). The low-energy cutoff was chosen individually for each detector; the number of protons below this cutoff was estimated by fitting a Gaussian to the low-energy tail of the Landau distribution.

The inclusive ΔE spectra resulting from conditions (i) and (ii) above are shown by the intermediate thin histogram in Fig. 7, whereas conditions (iii) and (iv) lead to the innermost (filled) histograms in Fig. 7. This procedure removed all breakup events in layers of matter other than the target and led to a practically background-free measurement.

The breakup protons lose only about 200 keV in the $300 \mu\text{m}$ thick SSD. Nevertheless, after imposing the vertex condition, the energy-deposition signals of protons in the SSD are clearly resolved from noise.

C. Invariant-mass reconstruction

1. Proton-ion opening angles

The p - ${}^7\text{Be}$ relative energy E_{rel} is derived from the total energies E of the particles, their 3-momenta p , and the p -Be

opening angle θ_{17} according to

$$E_{\text{rel}} = \sqrt{(E_{\text{Be}} + E_p)^2 - p_{\text{Be}}^2 - p_p^2 - 2p_{\text{Be}}p_p \cos(\theta_{17})}. \quad (1)$$

Whereas the proton and ${}^7\text{Be}$ momenta can be obtained only from the rather complicated momentum reconstruction procedure described in the next subsection, the p - ${}^7\text{Be}$ opening angle θ_{17} can be determined directly from constructing the vectors connecting the breakup vertex in the target with the corresponding hit positions in the SSD. Since protons fire only a single strip in each SSD, their positions are given by the strip centroid, and the variances of these positions—assuming that the hits are evenly distributed over the strip width—by the strip pitch, $100 \mu\text{m}$, divided by $\sqrt{12}$. In contrast, the larger energy deposits by the ${}^7\text{Be}$ ions produce broader hit patterns in our setup, with rather large fluctuations of the widths.

To reconstruct a breakup event, the p and ${}^7\text{Be}$ hits in each SSD have to be separated by at least one empty strip. Since this affects the efficiency for identifying a breakup event for low E_{rel} , we have to make sure that the GEANT simulation accurately reproduces this efficiency. This has been achieved by introducing a weighting function in GEANT that gradually increases the efficiency for detecting two separated hits from zero to 1 over the appropriate distance for each detector so that experimental and simulated distance distributions look alike. In Fig. 8, we plot the horizontal-distance distribution between proton and ${}^7\text{Be}$ hits in the first SSD. One can observe that experiment and simulation yield very similar distributions. It should be emphasized that in our earlier data analysis, a step function was assumed for this efficiency that jumped from zero to full efficiency at a fixed distance of 0.4 mm in each SSD. This is visualized by the dashed histogram in Fig. 8; it clearly shows that we overestimated the GEANT detection efficiency for small E_{rel} in our previous paper [13]. As we will show

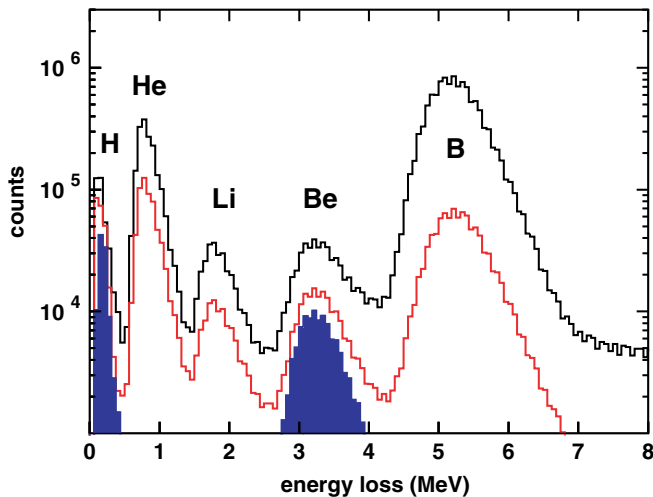


FIG. 7. (Color online) Energy deposition of the incident ${}^8\text{B}$ ions and of the breakup fragments in the third SSD. The outermost contour corresponds to all events. The intermediate thin contour depicts events where an incident ${}^8\text{B}$ particle is correlated with multiplicity $m = 2$ in each SSD. The innermost filled histograms are obtained by requiring a ΔE -cut on ${}^7\text{Be}$ in each SSD plus a p - ${}^7\text{Be}$ vertex inside the target volume (see text).

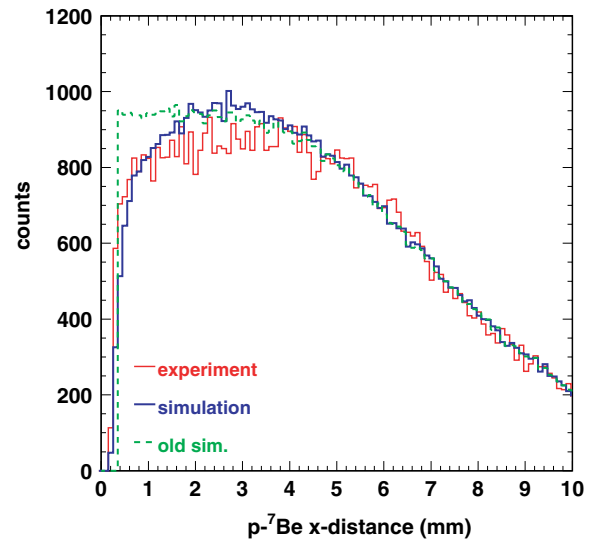


FIG. 8. (Color online) Horizontal (x) distances between proton and ${}^7\text{Be}$ hits in the first SSD. Thin (red) histogram shows the distribution of experimental distances; thick (blue) one, those from the present GEANT simulation. Dashed (green) histogram shows the GEANT simulation that was used to evaluate our previous results [13].

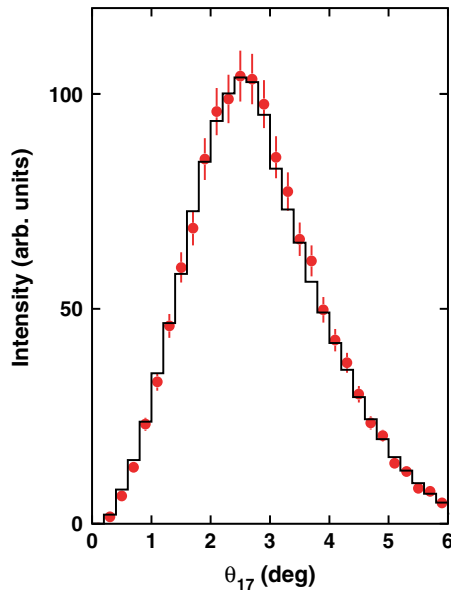


FIG. 9. (Color online) Distribution of opening angles between proton and ${}^7\text{Be}$, θ_{17} . Data points are shown by symbols; histogram indicates the GEANT simulation.

below, this leads to slightly larger cross sections at low E_{rel} compared to those of Ref. [13].

The validity of this procedure can be checked immediately by inspecting the integral distribution of p - ${}^7\text{Be}$ opening angles θ_{17} , both in experiment and in simulation. These distributions are shown in Fig. 9. The agreement is excellent.

2. Momentum reconstruction of the fragments

As mentioned already above, momenta for each particle (p , ${}^7\text{Be}$, ${}^8\text{B}$) were calculated from two position determinations in front of KaoS (in the SSD) and from another position determination behind KaoS (in the MWPC). These six coordinates were converted to momenta using three sets of 36-term polynomial expressions, one for each ion. By combining event by event the longitudinal momenta of p and ${}^7\text{Be}$, one can check the accuracy of the momentum reconstruction; its width is a measure of how well angular straggling effects are treated in the GEANT simulation. The comparison shows that the simulated momentum widths are more narrow by 20% compared to experiment. Therefore, the simulated σE_{rel} values shown in Fig. 6 (squares) were uniformly increased by 20% (circles).

D. Angular distributions

In the following, we will present some angular distributions that can be shown to be sensitive to an $E2$ amplitude in CD. Fig. 10 shows the coordinate systems used. With ${}^8\text{B}^*$ we denote the momentum vector of the (excited) ${}^8\text{B}$ prior to breakup, as it is reconstructed from the measured proton and ${}^7\text{Be}$ momentum vectors. The angle θ_8 is the laboratory scattering angle of ${}^8\text{B}^*$ relative to the incoming ${}^8\text{B}$ beam. The polar angles $\theta_{\text{c.m.}}$ and the azimuthal angles $\phi_{\text{c.m.}}$ of the breakup protons are measured in the rest frame of the ${}^8\text{B}^*$ system. In the same way, one

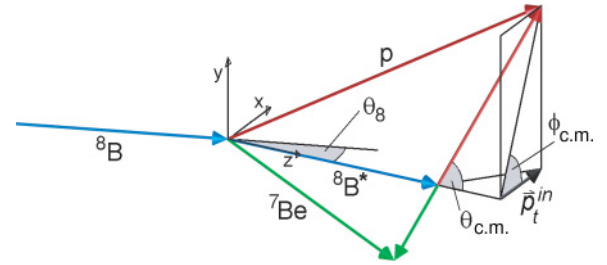


FIG. 10. (Color online) Vector diagram showing the definitions of the angles $\theta_{\text{c.m.}}$ and $\phi_{\text{c.m.}}$, as well as the proton inplane transverse momentum p_t^{in} in the frame of the ${}^8\text{B}^*$ system.

can calculate the transverse proton momentum vector in the reaction plane (p_t^{in}).

1. Comparison to perturbation theory calculations

Figure 11 shows the θ_8 distribution in comparison to two model calculations using first-order PT as discussed in Sec. II B. The full histogram denoting pure $E1$ multipolarity follows the data points very well, even to very large angles. The dashed histogram, where both $E1$ and $E2$ with their full theoretical strengths were assumed, deviates from the data points markedly for θ_8 values above about 0.7 degree. Note that the theoretical histograms were folded with the experimental response. We conclude that even the θ_8 distribution already indicates $E1$ dominance, in a similar way as that demonstrated in Kikuchi *et al.* [10].

We present in Fig. 12 the distribution of p_t^{in} for three different upper limits in θ_8 , 0.62° , 1.0° , and 2.5° . In classical Rutherford scattering, this corresponds to impact parameters of 30, 18.5, and 7 fm, respectively. Relative energies between p and ${}^7\text{Be}$ up to 1.5 MeV were selected. The experimental data for all three θ_8 cuts can be reproduced well by a PT calculation

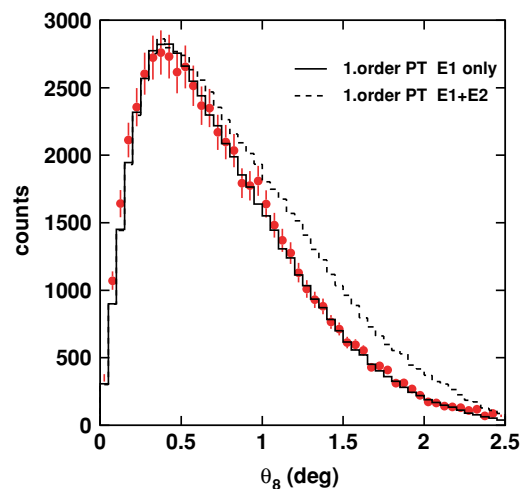


FIG. 11. (Color online) Scattering angle θ_8 of the excited ${}^8\text{B}$ prior to breakup, as reconstructed from the proton and ${}^7\text{Be}$ vectors. The full histogram has been calculated in first-order perturbation theory assuming pure $E1$ multipolarity; the dashed one, assuming $E1 + E2$ multipolarity.

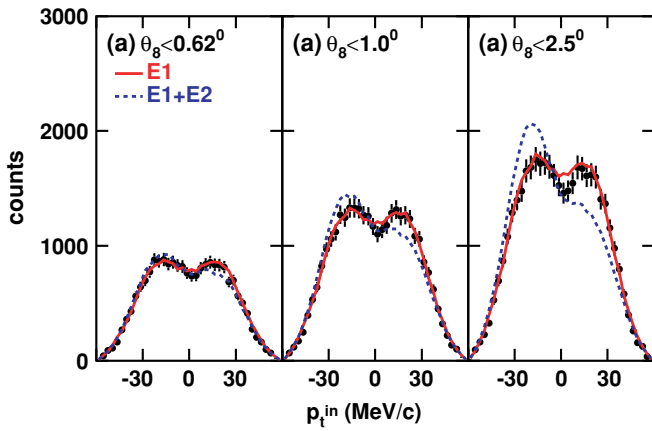


FIG. 12. (Color online) Inplane transverse momenta p_t^{in} of the breakup protons for three different cuts in θ_8 . Theoretical curves (full red lines: $E1$ multipolarity; dashed blue lines: $E1 + E2$ multipolarity) have been calculated in first-order perturbation theory. They were normalized individually to the data sets in each frame.

that includes only $E1$ multipolarity (full histograms in Fig. 12, the theoretical curves were normalized individually to the data sets). If $E1$ -plus- $E2$ multipolarity is used in the PT calculation, the different impact-parameter dependences of $E1$ and $E2$ multipolarity lead to markedly different shapes for the different θ_8 cuts (dashed histograms in Fig. 12). In particular for large values of θ_8 , the latter distributions show a large asymmetry with respect to $p_t^{\text{in}} = 0$ that is in clear disagreement with our data points.

By comparing Fig. 12 with similar plots in our earlier letter (Fig. 2 of Ref. [13]), one can see the improvement in the GEANT simulation achieved by the modified prescription for the p -Be hit resolution (see Sec. IV C1). The dips near $p_t^{\text{in}} \approx 0$ in the theoretical distributions are now much closer to the experimental ones (though small residual discrepancies are still visible in the rightmost panel).

Figure 13 depicts the experimental $\theta_{\text{c.m.}}$ distributions for three different E_{rel} bins, as indicated in the figure. A “safe” θ_8 limit of 1° was chosen. As expected, these distributions are mostly isotropic at low E_{rel} (indicative of s waves) and become increasingly anisotropic for larger values (contributions from higher orbital angular momenta). As in Fig. 12, also for the $\theta_{\text{c.m.}}$ distributions, the calculations for pure $E1$ multipolarity fit all spectra well; inclusion of an $E2$ component may lead to a slightly better fit at low E_{rel} , but diverges clearly for the large- E_{rel} bin where $E2$ should play a major role. The calculations with a dynamical model will be discussed below.

2. Comparison to dynamical calculations

As mentioned above, Esbensen *et al.* [30,31] suggested that dynamical calculations are required to properly describe CD and to evaluate S_{17} from the measured CD cross sections. A sensitive test to determine if such a theory describes the experimental data better than first-order PT calculations is given by comparing the dynamical predictions (using the model described in Sec. II B 2) to the same angular

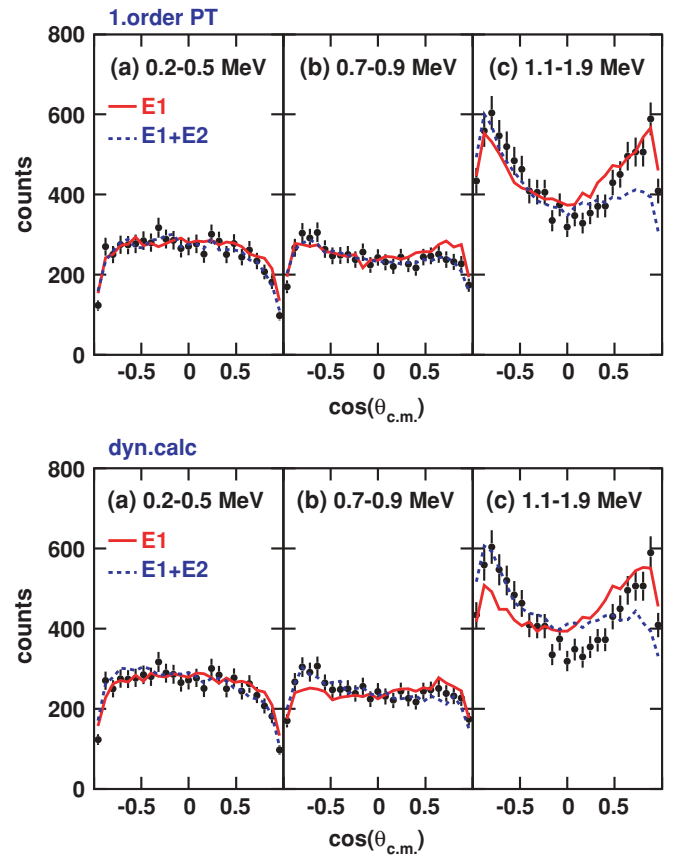


FIG. 13. (Color online) Top: Experimental proton polar angle $\theta_{\text{c.m.}}$ distributions for three different bins of the p - ${}^7\text{Be}$ relative energy E_{rel} . Full red curves denote a first-order PT calculation for $E1$ multipolarity; dashed blue ones for $E1 + E2$. All theoretical curves were individually normalized to the data points in each frame. Bottom: the same data compared to dynamical calculations, again for $E1$ (full curves) and for $E1 + E2$ (dashed curves) multiplicities (see text for details).

distributions (bottom part in Fig. 13). In all three frames shown, our $E1$ -only dynamical calculations do not agree well with the data points. Dynamical calculations with $E1 + E2$ seem to introduce a slight improvement as long as the effect of $E2$ multipolarity is small, but a major discrepancy shows up when $E2$ should have a stronger influence (rightmost lower panel in Fig. 13).

In general, one would expect that the more complete description of the Coulomb breakup within the semiclassical dynamical approach leads to better agreement with the experimental data than the simpler perturbative treatment. However, in the dynamical calculation, more model parameters that are not really constrained have to be specified than in the first-order approach. For example, the results for the angular distribution in the dynamical calculation depend crucially on the assumed $E2$ strength; i.e., there is a considerable model dependence. With sufficiently precise experimental data, it would be possible to determine this strength in a fitting procedure, but this requires extensive calculations. Additionally, one has to keep in mind that a full quantal treatment of the breakup process could lead to different results.

We conclude that within the limits of our experimental conditions, the simplest model (first-order PT with $E1$ multipolarity only) still gives the best agreement with the measured center-of-mass proton angular distributions. This is in line with conclusions drawn by Kikuchi *et al.* [10] and Iwasa *et al.* [12] from their respective θ_8 distributions (which are, however, less sensitive to a small $E2$ component than the present angular correlations). Our findings contradict the conclusions of Davids *et al.* [11] that a substantial $E2$ cross section has to be subtracted from the total measured CD cross section.

What remains to be done is to find a physical explanation for the small $E2$ strength compared to the model calculations (both the potential model and the cluster model predict almost equal S_{17}^{E2} values). At the same time, one has to find a different way to explain the asymmetries found in inclusive longitudinal-momentum distributions [11] and attributed either to a quenched [11] or enhanced [17,37,38] $E2$ strength relative to the respective model calculations.

E. Energy-differential dissociation yields

The measured momentum vectors of the outgoing p and ${}^7\text{Be}$ particles allowed us to calculate E_{rel} according to Eq. (1), from which we constructed the energy-differential dissociation yields of the excited ${}^8\text{B}^*$ system prior to breakup (Fig. 14). In line with our findings of a negligible $E2$ contribution discussed above, we compare this spectrum to a simulated one that contains contributions from $E1$ and $M1$ multipoles only. The latter contribution was calculated using the $M1$ resonance parameters as determined by Filippone *et al.* [22]. As expected,

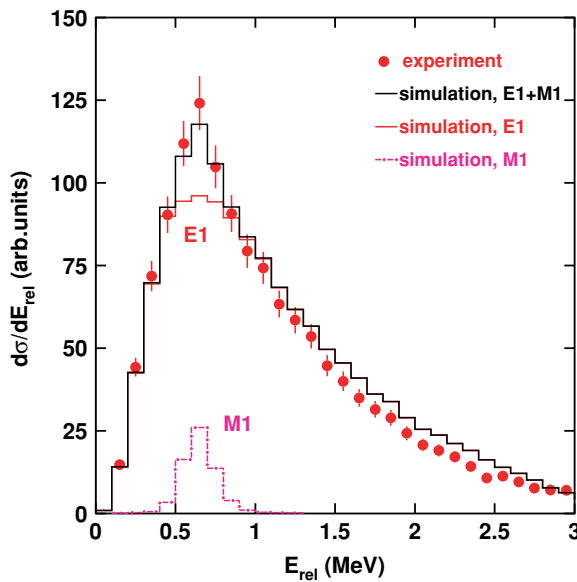


FIG. 14. (Color online) Energy-differential Coulomb-dissociation yields for equal-sized E_{rel} bins of 100 keV each. The thick outermost histogram results from our GEANT simulation including $E1$ and $M1$ multipolarity, scaled by a factor of 0.82. The thin (dash-dotted) histograms show the separate contributions from $E1$ ($M1$) multipolarity.

$M1$ contributes only in a narrow energy range around the peak of the spectrum. In plotting Fig. 14, we restricted the Rutherford scattering angles θ_8 to values below 1.0° to ensure both dominance of CD and reduction of the effect of any possible $E2$ contribution.

It should be noted that in CD, starting from the ${}^8\text{B}$ ground state, both the ground state and the first excited state at 429 keV in ${}^7\text{Be}$ can be observed as a result of first-order $E1$ excitation. The relative amount of these contributions to the CD are determined by the relative spectroscopic factors of the two ${}^7\text{Be}$ states in the ${}^8\text{B}$ ground state and the different photon spectra due to the different excitation energies. This component, which can be traced experimentally by observing the coincident 429 keV γ rays, needs to be subtracted before calculating S_{17} from differential CD cross sections. Numerical values for this branching have been kindly provided by Kikuchi *et al.* [10] and were scaled to the present bombarding energy using Weizsäcker-Williams theory.

Since the shape of the theoretical $d\sigma/dE$ distribution is better defined than its absolute magnitude, we normalized both distributions to each other; the resulting scaling factor is $f = 0.82$. With this renormalization, the experimental and simulated distributions agree rather well (Fig. 14). Small deviations between the data points and the histogram indicate discrepancies between the assumed S_{17} factor from our potential model and the true one, as will be discussed in the next section.

V. THE ASTROPHYSICAL S_{17} FACTOR

The measured quantity in CD of ${}^8\text{B}$ is the distribution of energy-differential cross sections, (Fig. 14). This distribution is related to S_{17} via a theoretical model. We assume that at the high incident energy used in our experiment and for the low Q value of the reaction, first-order perturbation theory is adequate to describe Coulomb dissociation. This has been investigated in detail in Ref. [27]. In analyzing our results, we also assume that the GEANT simulations describe all experimental effects quantitatively, in particular the feeding of neighboring bins due to the relatively bad E_{rel} resolution. We verified this assumption by comparing data and simulations for several raw observables, e.g., the θ_{17} distribution of Fig. 9 or the θ_8 distribution of Fig. 11. Based on the good agreement, we conclude that any remaining discrepancies between the two histograms in Fig. 14 can be attributed to a deviation of the true $E1$ S_{17} factor from the one used in our simulation. Thus, the true S_{17} factor for each bin was obtained by multiplying the theoretical one (averaged over this bin width) by the ratio of observed and simulated counts. The bins were chosen in accordance with the E_{rel} resolution (Fig. 6) to be roughly one FWHM wide, i.e., between 0.2 and 0.3 MeV. The resulting S_{17} factors as a function of E_{rel} are visualized in Fig. 15 and listed in Table I.

The error bars shown in Fig. 15 and listed in Table I contain all E_{rel} -dependent terms, resulting from counting statistics, from the error of the geometrical efficiency as determined by the GEANT simulations and from the error of the feeding of the excited state in ${}^7\text{Be}$. In addition, uncertainties in determining

TABLE I. Numerical values of S_{17} as a function of E_{rel} . The $1\text{-}\sigma$ errors include all E_{rel} -dependent terms. A common systematic error of 5.6% has to be added in quadrature to each data point (see text).

E_{rel} (MeV)	S_{17} (eV b)	$\sigma_{S_{17}}$ (eV b)
0.160	17.5	2.1
0.316	19.3	1.2
0.507	20.6	1.3
0.695	22.9	1.7
0.942	23.6	1.6
1.244	25.2	1.9
1.540	25.6	2.2
1.841	27.1	2.5
2.187	27.9	2.8
2.582	29.8	3.4
2.988	56.8	7.1

E_{rel} and θ_8 are included. An E_{rel} -independent systematic error of 5.6% has to be added for all data points, reflecting an estimated error of the dead-time correction (0.6%), the number of incident ${}^8\text{B}$ projectiles (1.4%), and the analysis (5.4%). The analysis error consists of the combined errors related to choosing the appropriate gates to identify a ${}^7\text{Be}$ fragment in the ΔE -TOF spectra (1.8%) and to identify a proton via the vertex reconstruction (5.1%). The latter contribution reflects the uncertainty in choosing the low-energy cutoff in the proton- ΔE spectra to remove the noise, which at the same time leads to the loss of some real proton events. More details can be found in Ref. [39].

A. Comparison with other CD experiments

Figure 15 shows the astrophysical S_{17} factors as deduced from the three other CD experiments published so far [10–12].

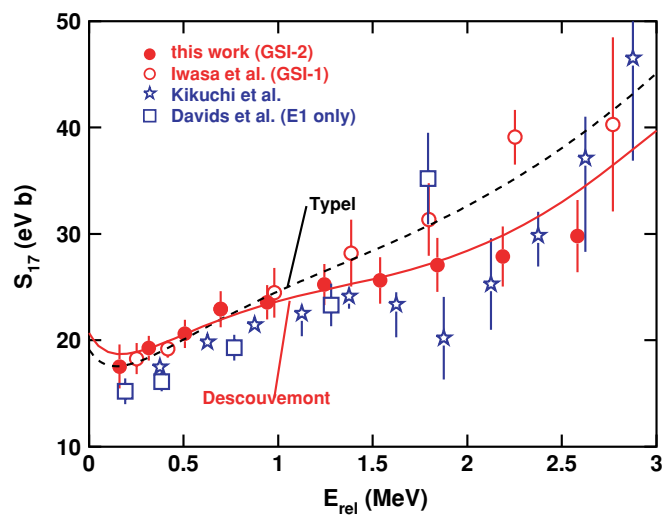


FIG. 15. (Color online) Comparison between S_{17} values from CD experiments. Full (open) circles indicate the present (previous) GSI CD experiment labeled GSI-2 (GSI-1). Open stars depict Ref. [10]; open squares, Ref. [11] ($E2$ contribution subtracted). The theoretical curves are described in the text.

(The data of Ref. [11] represent their $E1$ - S_{17} factors after subtraction of the $E2$ contribution.) The CD S_{17} factors are in reasonable agreement with each other, though both the Kikuchi *et al.* [10] and the Davids *et al.* [11] data are systematically lower. We note that also our earlier CD experiment [12] and the present one are in good agreement up to $E_{\text{rel}} \approx 1.5$ MeV; marked discrepancies occur only at higher E_{rel} values. Compared to our previous results given in Ref. [13], the lowest three data points have been increased by 6.7%, 10%, and 5.8%, respectively. The remaining data points remain largely unaffected. As a consequence, the slope of our S_{17} factors as a function of E_{rel} becomes smaller and fits much better than previously to the energy dependence of Descouvemont's cluster model; we will discuss this aspect in more detail below.

In the above comparison with other published CD results, we plotted S_{17} values as deduced by the authors in their analyses. Other evaluations of the same data sets may lead to different results. An example is the recent reanalysis of the energy- and angle-differential cross sections, $d\sigma/dE$ and $d\sigma/d\theta_8$, of the RIKEN-2 experiment [10] by Ogata *et al.* [40]. The former authors deduced a zero-energy factor of $S_{17}(0) = 18.9 \pm 1.8$ eV b based on first-order perturbation theory. Ogata *et al.* obtained $S_{17}(0) = 21.4^{+2.0}_{-1.9}$ eV b from the same experimental data by taking into account the interference of nuclear, $E1$, and $E2$ contributions and higher-order processes.

B. Comparison with direct-capture experiments

Figure 16 compares our data to those of the recent ${}^7\text{Be}(p, \gamma){}^8\text{B}$ measurements in which the authors subtracted the contribution from the $M1$ resonance [5,7,8]. (Since we

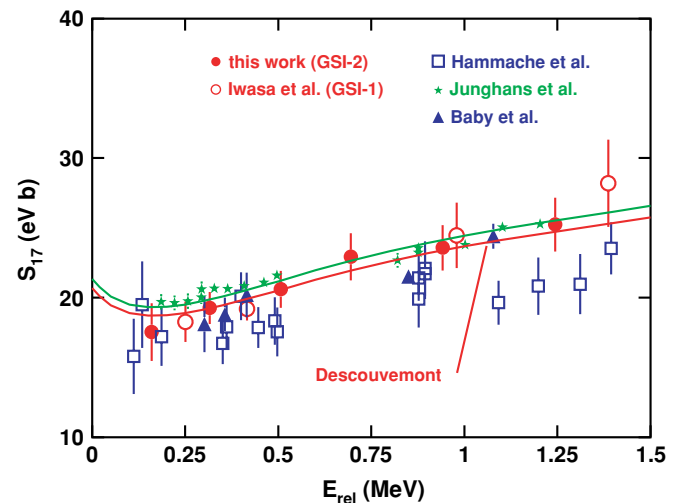


FIG. 16. (Color online) S_{17} from this work in comparison with the (p, γ) experiments of Ref. [5] (squares), Ref. [8] (stars), and Ref. [7] (triangles). The latter data were corrected for the contribution of the $M1$ resonance by the authors. The theoretical curves are from Descouvemont [18] and have been fitted to the Seattle data (upper curve, Ref. [8]) and the present data (lower curve). See text for more details.

do not intend to dwell on discrepancies among the results from direct-proton-capture experiments, we restrict ourselves to the three data sets shown). With the modifications of the lowest- E_{rel} data points discussed above, our data set now follows closely the (p, γ) data of Junghans *et al.* [8] over their *entire* energy range. Previously [13] we noted good agreement with [7,8] only for the data points above the $M1$ resonance. This partly solves a puzzle that Junghans *et al.* claim to have observed, a systematic discrepancy between the slope of the CD S_{17} factors and those from direct- p -capture experiments. It also removes the experimental basis for recommendations by Esbensen *et al.* [31] to modify the deduced slope of $S_{17}(E_{\text{rel}})$ on the basis of a fully dynamical calculation.

C. Extrapolation to zero relative energy

To extrapolate to zero energy, all recent (p, γ) experiments have chosen the cluster model of Descouvemont and Baye [9]. As mentioned above, Descouvemont [18] recently refined the cluster-model description of ${}^8\text{B}$ (we refer to this model below as D04). In this refined approach, the curve resulting from the Minnesota force (MN) is closer to the experimental data and was used in Fig. 16 to fit both the Seattle data [8] and our present results over the energy range up to $E_{\text{rel}} = 1.5$ MeV. The fits yield practically identical results within their respective errors. The D04 normalization factor for our data set is 0.837 ± 0.013 with a reduced χ^2 of 0.40. Note that Descouvemont investigated the error introduced by scaling the S factor and found it negligible [18].

Our previous data set [13] proved to be most compatible with the potential-model calculation of Typel as discussed in Sec. II B of the present paper or in Davids and Typel [17] (referred to below as DT03). It is obvious that with the modified low-energy data points of the present paper, the agreement with this model is less satisfactory. The black dashed curve in Fig. 15 visualizes a fit of this theory to our data. Though from a purely statistical point of view the fit with the DT03 curve is acceptable, we prefer to describe our data with the D04 theory for the following reasons:

- (i) The two-cluster structure of ${}^7\text{Be}$ is related to its intrinsic deformation, so a model of ${}^8\text{B}$ based on this feature should be more realistic.
- (ii) The S_{17} energy dependence from all modern direct- p -capture experiments can be described consistently and fitted with high confidence with the cluster model, thus corroborating the above conjecture.
- (iii) D04 allows us to fit our lower four to nine data points with practically equal results; i.e., the scaling factor does not depend on the fit range. In contrast, the DT03 scaling

factor changes continuously with increasing fit range, reflecting the different shape of the curve.

- (iv) Using D04, we find $\chi_{\text{red}}^2 < 1$ for a fit range up to 2 MeV; the DT03 fit yields $\chi_{\text{red}}^2 > 1$ already if the fit range is extended above 1.3 MeV.

When we fit our lowest eight data points, up to $E_{\text{rel}} = 2$ MeV, to the D04 model, we obtain $S_{17}(0) = 20.6 \pm 0.8$ eV b. The same result within error bars is obtained if we use any number of data points between four and eight. As mentioned above, a systematic error of 5.6% has to be added, yielding $S_{17}(0) = 20.6 \pm 0.8(\text{stat}) \pm 1.2(\text{syst})$ eV b. Not included in these numbers is the theoretical uncertainty given by Descouvemont [18] as 5–10% depending on the relative energy.

This result overlaps perfectly with a fit of D04 to the full data set of Junghans *et al.* [8] which gives $S_{17}(0) = 21.2 \pm 0.5$ eV b. A fit of the Baby *et al.* [7] (p, γ) data to the D04 model yields a very similar result, $S_{17}(0) = 19.8 \pm 1.0$ eV b. When fitting D04 to the Hammache *et al.* [5] data set, we obtain a smaller central value of $S_{17}(0) = 18.4 \pm 1.7$ eV b, but the error bar still overlaps with ours.

VI. CONCLUSIONS

We conclude that at sufficiently high incident energy, a high-resolution exclusive Coulomb-dissociation experiment can provide a rather precise value for the low-energy ${}^7\text{Be}(p, \gamma){}^8\text{B}$ cross section. Among other conditions to be fulfilled, the efficiency of the method as a function of proton- ${}^7\text{Be}$ relative energy has to be modeled precisely. By setting tight constraints to the scattering angle θ_8 and analyzing proton- ${}^7\text{Be}$ angular correlations, a significant contribution from $E2$ multipolarity could be excluded. Compared to our first study of ${}^8\text{B}$ Coulomb dissociation [12], we could base this conclusion on carefully measured angular distributions. In contrast to our earlier publication [13], our reanalyzed results for the astrophysical S_{17} factor follow closely the energy dependence as predicted by the refined cluster-model description of Descouvemont [18]. This finding is in line with the most recent measurements of the ${}^7\text{Be}(p, \gamma){}^8\text{B}$ reaction. The combined statistical and systematic errors of our fit value for $S_{17}(0)$ amount to 6.6%; a similar error contribution of about 5% comes from the model uncertainty [18].

ACKNOWLEDGMENTS

The authors thank K.-H. Behr, K. Burkard, and A. Brünle for technical assistance. Vivid discussions with B. Davids, P. Descouvemont, M. Hass, and A. Junghans are gratefully acknowledged.

[1] Q. R. Ahmad *et al.*, Phys. Rev. Lett. **89**, 011301 (2002); **89**, 011302 (2002).
 [2] B. Aharmim *et al.*, Phys. Rev. C **72**, 055502 (2005).
 [3] J. N. Bahcall and M. H. Pinsonneault, Phys. Rev. Lett. **92**, 121301 (2004).

[4] S. Turck-Chieze, S. Couvidat, L. Piau, J. Ferguson, P. Lambert, J. Ballot, R. A. Garcia, and P. Nghiem, Phys. Rev. Lett. **93**, 211102 (2004).
 [5] F. Hammache *et al.*, Phys. Rev. Lett. **86**, 3985 (2001).
 [6] F. Strieder *et al.*, Nucl. Phys. **A696**, 219 (2001).

- [7] L. T. Baby *et al.*, Phys. Rev. Lett. **90**, 022501 (2003).
[8] A. R. Junghans *et al.*, Phys. Rev. C **68**, 065803 (2003).
[9] P. Descouvemont and D. Baye, Nucl. Phys. **A567**, 341 (1994).
[10] T. Kikuchi *et al.*, Phys. Lett. **B391**, 261 (1997); Eur. Phys. J. A **3**, 213 (1998).
[11] B. Davids, S. M. Austin, D. Bazin, H. Esbensen, B. M. Sherrill, I. J. Thompson, and J. A. Tostevin, Phys. Rev. C **63**, 065806 (2001).
[12] N. Iwasa *et al.*, Phys. Rev. Lett. **83**, 2910 (1999).
[13] F. Schümann *et al.*, Phys. Rev. Lett. **90**, 232501 (2003).
[14] A. M. Mukhamedzhanov, C. A. Gagliardi, and R. E. Tribble, Phys. Rev. C **63**, 024612 (2001).
[15] L. Trache, F. Carstoiu, C. A. Gagliardi, and R. E. Tribble, Phys. Rev. C **69**, 032802(R) (2004).
[16] D. Cortina-Gil *et al.*, Nucl. Phys. **A720**, 3 (2003).
[17] B. Davids and S. Typel, Phys. Rev. C **68**, 045802 (2003).
[18] P. Descouvemont, Phys. Rev. C **70**, 065802 (2004).
[19] D. R. Tilley *et al.*, Nucl. Phys. **A745**, 155 (2004).
[20] L. Koester, K. Knopf, and W. Waschkowski, Z. Phys. A **312**, 81 (1983).
[21] C. Angulo *et al.*, Nucl. Phys. **A716**, 211 (2003).
[22] B. W. Filippone, A. J. Elwyn, C. N. Davids, and D. D. Koetke, Phys. Rev. C **28**, 2222 (1983).
[23] F. M. Nunes, R. Crespo, and I. J. Thompson, Nucl. Phys. **A615**, 69 (1997).
[24] G. Baur, C. A. Bertulani, and H. Rebel, Nucl. Phys. **A458**, 188 (1986).
[25] K. Alder, A. Bohr, T. Huus, B. Mottelson, and A. Winther, Rev. Mod. Phys. **28**, 432 (1956).
[26] C. A. Bertulani, Phys. Rev. C **49**, 2688 (1994); Z. Phys. A **356**, 293 (1996).
[27] S. Typel, H. H. Wolter, and G. Baur, Nucl. Phys. **A613**, 147 (1997), implemented as code CDXS by S. Typel (2002).
[28] A. Winther and K. Alder, Nucl. Phys. **A319**, 518 (1979).
[29] C. A. Bertulani and M. Gai, Nucl. Phys. **A636**, 227 (1998).
[30] H. Esbensen, Phys. Rev. C **70**, 047603 (2004).
[31] H. Esbensen, G. F. Bertsch, and K. A. Snover, Phys. Rev. Lett. **94**, 042502 (2005).
[32] E. O. Alt, B. F. Irgaziev, and A. M. Mukhamedzhanov, Phys. Rev. C **71**, 024605 (2005).
[33] H. Geissel *et al.*, Nucl. Instrum. Methods Phys. Res. B **70**, 286 (1992).
[34] H. Kumagai *et al.*, Nucl. Instrum. Methods Phys. Res. A **470**, 562 (2001).
[35] P. Senger *et al.*, Nucl. Instrum. Methods Phys. Res. B **327**, 393 (1993).
[36] GEANT Detector Description and Simulation Tool, CERN Program Library Long Writeup W5013 (1993).
[37] J. Mortimer, I. J. Thompson, and J. A. Tostevin, Phys. Rev. C **65**, 064619 (2002).
[38] N. C. Summers and F. M. Nunes, J. Phys. G: Nucl. Part. Phys. **31**, 1437 (2005).
[39] F. Schümann, Ph.D. thesis, Ruhr-Universität Bochum, 2002; <http://www.ep3.ruhr-uni-bochum.de/~schuemann/dissertation.htm> (in German).
[40] K. Ogata *et al.*, nucl-th/0505007, Phys. Rev. C (to be published).